www.solar-rrl.com

Validated Method for Evaluating the Four-Terminal Perovskite/Si Tandem Cell Performance and its Efficiency Potential

Dong Zhang, Kunal Datta, Valerio Zardetto, Sjoerd Veenstra, Gianluca Coletti, and René A. J. Janssen*

Recently perovskite/crystalline Si (cSi) tandem cells draw considerable attention because their high efficiency can reduce the levelized cost of electricity and increase the power density of photovoltaics (PVs) to accelerate the energy transition. While the theoretical limits for tandem cells are well known, the practical limits are less clear. Herein, a new method is presented to calculate the efficiency of a four-terminal (4T) tandem based on the performance of single-junction perovskite and cSi cells, using their detailed-balance efficiency fraction. This calculation method is validated with experiments on 4T perovskite/cSi tandem cells that provide a maximum efficiency of 28.0% and with the literature data available for similar configurations. A maximum efficiency of about 36% is estimated for 4T perovskite/cSi tandem cells that would use present record perovskite and cSi PV cells. This can be regarded as the practical efficiency limit for 4T perovskite/cSi tandem devices.

D. Zhang, K. Datta, R. A. J. Janssen Molecular Materials and Nanosystems Institute for Complex Molecular Systems Eindhoven University of Technology Partner in Solliance 5600 MB Eindhoven, The Netherlands E-mail: r.a.j.janssen@tue.nl

D. Zhang, V. Zardetto, S. Veenstra, G. Coletti TNO $\,$

Partner in Solliance 5656 AE Eindhoven, The Netherlands

G. Coletti School of Photovoltaic and Renewable Energy Engineering University of New South Wales Sydney NSW 2052, Australia

R. A. J. Janssen Dutch Institute for Fundamental Energy Research 5612 AJ Eindhoven, The Netherlands

The ORCID identification number(s) for the author(s) of this article can be found under https://doi.org/10.1002/solr.202200914.

© 2022 The Authors. Solar RRL published by Wiley-VCH GmbH. This is an open access article under the terms of the Creative Commons Attribution License, which permits use, distribution and reproduction in any medium, provided the original work is properly cited.

DOI: 10.1002/solr.202200914

1. Introduction

The increase of the power conversion efficiency (η) of solar cells can effectively reduce the levelized cost of electricity (LCOE) of photovoltaics (PVs) especially because the fraction of balance of system (BOS) increases up to about 70% of the total cost of PV systems nowadays.[1] However, the efficiency of crystalline Si (cSi) cells as the mainstream PV technology is approaching its practical limit. [2,3] By adding a widebandgap cell on top of a cSi cell to form a tandem cell, the theoretical limit of a singlejunction solar cell can be surpassed.^[4] The theoretical limit is calculated based on the detailed-balance model^[5] and often referred to as the detailed-balance limit. Figure 1 shows the detailed-balance

efficiency limit of a single-junction solar cell as a function of bandgap energy (E_g) . The optimal range for E_g lies between 1.1 and 1.4 eV and the highest efficiency is 33.1%. [6,7] When a top cell with larger E_g is used to form a tandem with a cSi cell, much higher efficiency up to 44.7%^[8] can be reached when E_{σ} is about 1.81 eV. The four-terminal (4T) tandem, as one of the tandem configurations, has several advantages over its two-terminal (2T) counterpart. Most relevant is that a 4T configuration is not limited by current matching, implying that it is less sensitive to spectral changes and flexible for bifacial application with varying albedo. ^[9] The 4T configuration also allows separate optimization of subcells and simple mechanical stacking of them for module assembly. In principle, the perovskite subcell in the 4T configuration can be applied as an add-on, and therefore requires minimal adaption in the cSi cell processing or device layout. In contrast, the disadvantages of a 4T tandem cell include the demand for an additional transparent conductive oxide (TCO) electrode compared to the 2T tandem cell, implying extra module cost. In addition, module integration and 4T electrical connection on the module and system levels, which involves doubling the power electronics, are not as straightforward as it might appear for 2T.[10,11] Concerning the cell efficiency, 2T and 4T tandems have nearly the same theoretical maximum,[12] although in practice over 29% has been reached for the 4T tandem^[13] and over 31% has been reached for the 2T tandem. [14]

Rapid development of perovskite/cSi tandem cells benefits from the research progress in single-junction perovskite and

ns) on Wiley Online Library for rules of use; OA articles are governed by the applicable Creative Commons License

www.solar-rrl.com

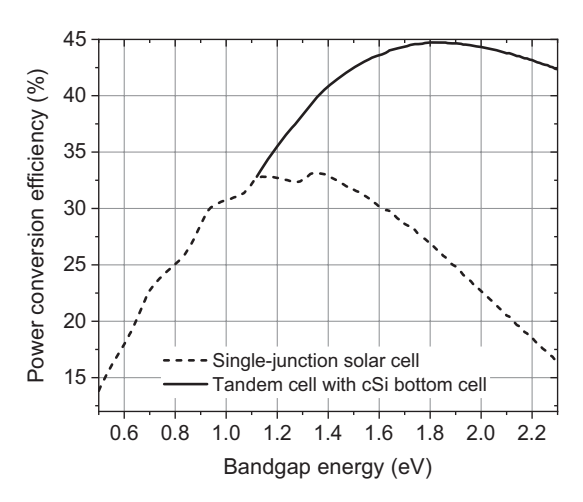


Figure 1. Theoretical efficiency calculated for a single-junction solar cell as a function of the bandgap energy $E_{\rm g}$ and for a 4T tandem cell comprising a crystalline Si (cSi) bottom cell as a function of $E_{\rm g}$ of the top cell. The calculations are based on the detailed-balance theory and are explained in Section 1, Supporting Information.

cSi cells. The general strategy for optimizing 4T perovskite/cSi tandem cells includes efficiency improvement of the perovskite top and cSi bottom cells, enhancement of the near-infrared (NIR) transmission of the perovskite top cell, and tuning of the

perovskite bandgap energy ($E_{\rm g,PER}$). However, how these optimization aspects quantitatively contribute to the performance of the tandem cell has not been discussed in the literature. In this contribution, we fabricate and characterize a 28.0%-efficient 4T perovskite/cSi tandem cell. Furthermore, we introduce a method to calculate the 4T tandem efficiency and validate it by comparing the calculated and experimental values, both from data generated in-house and data available in the literature. This method quantitatively connects the 4T tandem efficiency to the aforementioned optimization aspects giving a clear path to focus on the research efforts.

2. Results and Discussion

2.1. Fabrication and Characterization of 4T Perovskite/cSi Tandem Cell

Semitransparent perovskite solar cells (ST-PSCs), i.e., the top cells of the 4T tandem, were processed on glass substrates covered with two different TCOs. One has hydrogenated indium oxide (IOH) as a front electrode and is named ST-PSC-1, while the other has indium tin oxide (ITO) as front TCO and is named ST-PSC-2. Details of the device fabrication and characterization methods are provided in the Experimental Section. Figure 2 shows the photovoltaic characterization of the two cells and Table 1 contains the relevant photovoltaic parameters. Both

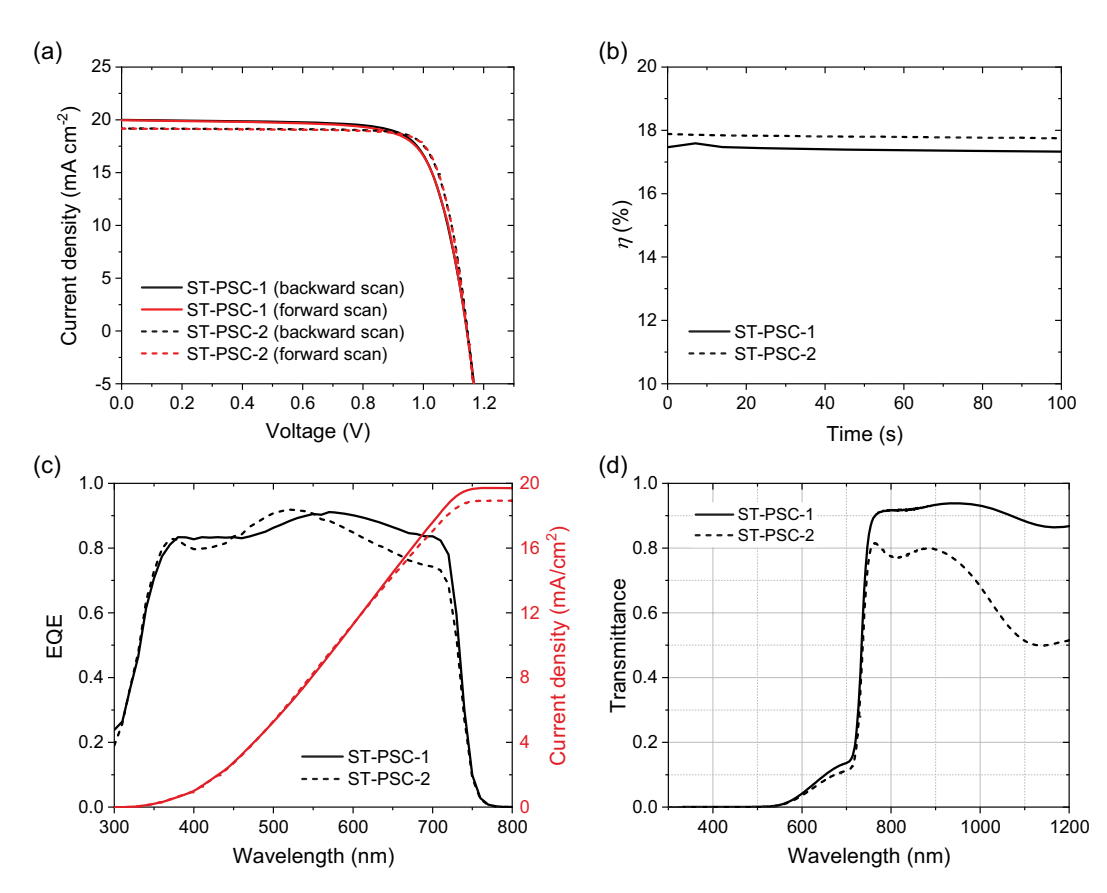


Figure 2. Photovoltaic (PV) characterization of the semitransparent perovskite solar cells with an IOH (ST-PSC-1) and an ITO (ST-PSC-2) front electrode. a) *J*–V curves. b) Maximum power point tracking (MPPT). c) External quantum efficiency (EQE) spectra. d) Transmittance spectra.

Solar

www.solar-rrl.com

Table 1. J–V parameters of 4T tandem cells with different ST-PSCs and the same MWT-SHJ cSi cell.

| Cell | Description | V _{oc} [mV] | $J_{\rm sc}$ [mA cm $^{-2}$] | FF [%] | η [%] |
|---|----------------------|-------------------------|-------------------------------|-----------|----------|
| ST-PSC-1 (E _{g,PER} : 1.69 eV) | Backward scan | 1145 | 20.0 | 76.0 | 17.4 |
| | Forward scan | 1145 | 20.0 | 75.3 | 17.2 |
| | MPPT | _ | - | - | 17.3 |
| cSi-cell (MWT-SHJ) | Single junction | 731 | 39.8 | 78.1 | 22.7 |
| | Filtered by ST-PSC-1 | 717 | 18.8 | 79.5 | 10.7 |
| Tandem-1 | | | | | 28.0 |
| ST-PSC-2 (E _{g,PER} : 1.69 eV) | Backward scan | 1146 | 19.2 | 80.7 | 17.8 |
| | Forward scan | 1145 | 19.2 | 80.8 | 17.8 |
| | MPPT | - | - | - | 17.8 |
| cSi-cell (MWT-SHJ) | Single junction | 731 | 39.8 | 78.1 | 22.7 |
| | Filtered by ST-PSC-2 | 711 | 15.0 | 79.8 | 8.5 |
| Tandem-2 | | | | | 26.3 |

ST-PSC-1 and ST-PSC-2 have negligible hysteresis in the current density-voltage (I-V) characteristics (Figure 2a) and are stable during 100 s of maximum power point tracking (MPPT) (Figure 2b). Both Figure 2a and the external quantum efficiency (EQE) spectrum (Figure 2c) indicate that ST-PSC-1 provides a higher short-circuit current density (Isc) than ST-PSC-2 mainly because the parasitic absorption of IOH is much smaller than that of ITO (Figure S1, Supporting Information). The reduced parasitic absorption of IOH as TCO also results in a higher transparency of the ST-PSC-1 cell in the NIR compared to the ST-PSC-2 cell as shown in Figure 2d. It is noted that ST-PSC-1 has a lower fill factor (FF) than ST-PSC-2. This could be related to the work function difference between ITO and IOH as reported by Semma et al.[16] Zhao et al. reported that the TCO work function can affect the depletion region of the p-n junction in silicon heterojunction solar cells, consequently influencing the cell performance. [17] Similar effects of the TCO work function could be applicable to the hole transport layer (HTL)/perovskite interface. This possible explanation has not been studied in detail, and therefore requires further investigation.

By combining these ST-PSCs with a metal-wrap through silicon heterojunction (MWT-SHJ) bottom cell, it is possible to characterize the performance of the corresponding 4T tandem cell. Figure 3 shows the schematic layout of the 4T perovskite/ cSi tandem cells. Since the ST-PSC and MWT-SHJ bottom cells have very different areas, the protocol for 4T tandem measurement published by Werner et al. [18] was used as described in the Experimental Section. The results of the 4T tandem characterization are summarized in Table 1. Although the ST-PSC-2 single-junction cell performs slightly better than the ST-PSC-1 cell, the efficiency of Tandem-1 is much higher as a consequence of the higher NIR transparency of ST-PSC-1. The efficiency of the 4T-tandem cell that combines a ST-PSC-1 top cell with an MWT-SHJ bottom cell is 28.0%. The *J*–*V* curve and EQE spectrum of the MWT-SHJ bottom cell are shown in Figure S2, Supporting Information.

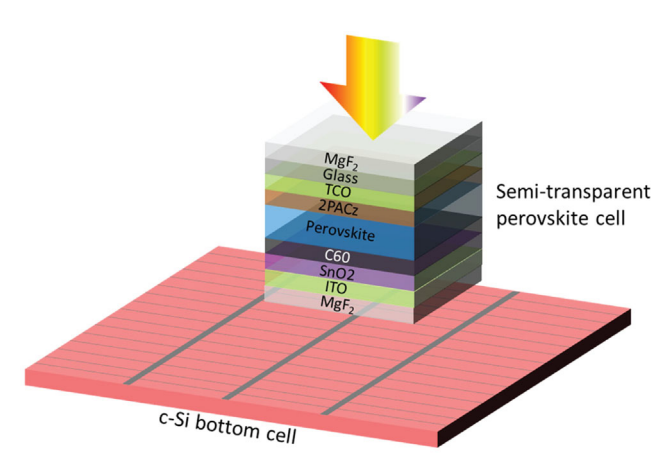


Figure 3. Schematic layout of the 4T perovskite/cSi tandem cells in this study. The tandem configuration includes a small ST-PSC (aperture area of 9 mm²) top cell and a 6 inch cSi bottom cell. The TCO on the glass is either IOH or ITO. There is an air gap between the top and bottom cells.

While the differences between Tandem-1 and Tandem-2 can be easily understood in qualitative terms, the question arises whether they be accurately predicted in quantitative terms based on the characteristics of the individual subcells. In the following, we describe a method to predict the efficiency of a 4T tandem, based on few measurable characteristics of the top and bottom subcells, and then use it to determine a practical efficiency limit for 4T perovskite/cSi tandem cells based on current record top and bottom cells.

2.2. Method to Calculate the 4T Tandem Efficiency and its Validation

The model starts by relating the actual performance of a single-junction perovskite cell, i.e., the open-circuit voltage ($V_{\text{oc,PER}}$), short-circuit current density ($J_{\text{sc,PER}}$), fill factor (FF_{PER}), and efficiency (η_{PER}) of the perovskite and the cSi cell ($V_{\text{oc,cSi}}$, $J_{\text{sc,cSi}}$, FF_{cSi}, and η_{cSi}) to their detailed-balance performance limits at their corresponding bandgap energies expressed by the following fractions (f)

$$\begin{cases} f_{\text{PER}}(E_{\text{g,PER}}) = \frac{\eta_{\text{PER}}}{\eta_{\text{PER}}^{\text{t}}(E_{\text{g,PER}})} \\ f_{\text{Voc,PER}}(E_{\text{g,PER}}) = \frac{V_{\text{oc,PER}}}{V_{\text{oc,PER}}^{\text{t}}(E_{\text{g,PER}})} \end{cases} \qquad \begin{cases} f_{\text{cSi}} = \frac{\eta_{\text{cSi}}}{\eta_{\text{cSi}}^{\text{t}}} \\ f_{\text{Voc,cSi}} = \frac{V_{\text{oc,CSi}}}{V_{\text{oc,CSi}}^{\text{t}}} \end{cases} \\ f_{\text{Jsc,PER}}(E_{\text{g,PER}}) = \frac{J_{\text{sc,PER}}(E_{\text{g,PER}})}{J_{\text{sc,PER}}^{\text{t}}(E_{\text{g,PER}})} \end{cases} \qquad \begin{cases} f_{\text{cSi}} = \frac{\eta_{\text{cSi}}}{\eta_{\text{cSi}}^{\text{t}}} \\ f_{\text{Voc,cSi}} = \frac{V_{\text{oc,CSi}}}{V_{\text{oc,CSi}}} \end{cases} \end{cases} \\ f_{\text{Jsc,cSi}} = \frac{J_{\text{sc,CSi}}}{J_{\text{sc,CSi}}^{\text{t}}} \\ f_{\text{FF,PER}}(E_{\text{g,PER}}) = \frac{FF_{\text{pER}}}{FF_{\text{PER}}^{\text{t}}(E_{\text{g,PER}})} \end{cases} \end{cases}$$

$$f_{\text{PER}}(E_{\text{g,PER}}) = f_{\text{Voc,PER}}(E_{\text{g,PER}}) \cdot f_{\text{Jsc,PER}}(E_{\text{g,PER}}) \cdot f_{\text{FF,PER}}(E_{\text{g,PER}})$$
(2)

$$f_{cSi} = f_{Voc,cSi} \cdot f_{Isc,cSi} \cdot f_{FF,cSi}$$
(3)

where $V_{\text{oc,PER}}^{\text{t}}$, $J_{\text{sc,PER}}^{\text{t}}$, $FF_{\text{PER}}^{\text{t}}$, and $\eta_{\text{PER}}^{\text{t}}$ are the theoretical (t) detailed-balance performance limits for the perovskite cell,

www.advancedsciencenews.com www.solar-rrl.com

and $V_{oc,cSi}^t$, $J_{sc,cSi}^t$, FF_{cSi}^t , and η_{cSi}^t are the corresponding values for the cSi cell. f_{PFR} and f_{cSi} represent the ratios of the actual efficiencies of the two cells relative to their detailed-balance limits. The calculation of the detailed-balance performance limit is explained in detail in Section 1, Supporting Information. The performance of an ST-PSC measured as a single-junction device is almost identical to its performance on top of the cSi cell in a 4T tandem configuration. Although the cSi cell can reflect part of transmitted photons with energies larger than $E_{g,PER}$, the effect of back reflection is negligible. The reasons are that the number of transmitted photons is very limited due to the high absorption coefficients of the perovskite^[19] and that the reflectivity of cSi cells is very small due to optimized antireflection. [20] In contrast, the performance of the cSi bottom cell in the 4T tandem differs significantly from the performance of the same cell in a single-junction configuration because the cSi bottom cell is optically filtered by the perovskite top cell. Similar to the variables defined for the single-junction cell, the filtered cSi bottom cell is defined with $V_{
m oc,bot}$, $J_{
m sc,bot}$, FF $_{
m bot}$, and $\eta_{
m bot}$ for the actual performance, $V_{\text{oc bot}}^{\text{t}}, J_{\text{sc bot}}^{\text{t}}, \text{FF}_{\text{bot}}^{\text{t}}, \text{ and } \eta_{\text{bot}}^{\text{t}}$ for the detailed-balance performance limit, and $f_{\text{Voc,bot}}$, $f_{\text{Jsc,bot}}$, $f_{\text{FF,bot}}$, and f_{bot} for the ratios of the two parameter sets. The actual 4T tandem efficiency (η_{4T}) can then be expressed by the following equations

$$\eta_{\text{4T}} = \eta_{\text{PER}} + \eta_{\text{bot}} = f_{\text{PER}} \cdot \eta_{\text{PER}}^{\text{t}} + f_{\text{bot}} \cdot \eta_{\text{bot}}^{\text{t}}
= f_{\text{PER}} \cdot \eta_{\text{PER}}^{\text{t}} + f_{\text{Voc,bot}} \cdot f_{\text{Isc,bot}} \cdot f_{\text{FF,bot}} \cdot \eta_{\text{bot}}^{\text{t}}$$
(4)

$$f_{\text{Voc,bot}} = \frac{V_{\text{oc,bot}}}{V_{\text{oc,bot}}^{\text{t}}} = \frac{\frac{nkT}{e} \ln \left(\frac{J_{\text{sc,bot}}}{J_{\text{0,cSi}}}\right)}{\frac{kT}{e} \ln \left(\frac{J_{\text{sc,bot}}^{\text{t}}}{J_{\text{0,cSi}}^{\text{t}}}\right)} = \frac{n \ln \left(\frac{aJ_{\text{sc,cSi}}}{J_{\text{0,cSi}}}\right)}{\ln \left(\frac{bJ_{\text{sc,cSi}}}{J_{\text{0,cSi}}}\right)}$$

$$= \frac{n \ln\left(\frac{J_{\text{sc,cSi}}}{J_{0,\text{csi}}}\right) + n \ln a}{\ln\left(\frac{J_{\text{sc,cSi}}}{J_{0,\text{csi}}}\right) + \ln b} \approx \frac{n \ln\left(\frac{J_{\text{sc,cSi}}}{J_{0,\text{csi}}}\right)}{\ln\left(\frac{J_{\text{sc,cSi}}}{J_{0,\text{csi}}}\right)} = f_{\text{Voc,cSi}}$$
(5)

where $J_{0,cSi}$ is the actual saturation current density of the cSi cell and $J_{0,cSi}^{t}$ its theoretical value based on the detailed-balance limit.

Further, n is the ideality factor, e is the elemental charge, and aand b are equal to $J_{\text{sc,bot}}/J_{\text{sc,cSi}}$ and $J_{\text{sc,bot}}^{\text{t}}/J_{\text{sc,Si}}^{\text{t}}$, respectively, and therefore, related to $E_{\rm g,PER}$ and the transmittance of the perovskite top cell. Figure S3, Supporting Information shows the value of $J_{\text{sc bot}}^{\text{t}}/J_{\text{sc cSi}}^{\text{t}}$ as a function of $E_{\text{g,PER}}$ and the transmittance of the perovskite top cells. The range for $E_{\rm g,PER}$ (1.6 $\leq E_{\rm g,PER} \leq$ 2.3 eV) and for the transmittance $(0.7 \le T \le 1.0)$ used in Figure S3, Supporting Information, were chosen because $E_{g,PER} > 1.6 \text{ eV}$ is commonly used for perovskite/cSi tandem cells and a transmittance above 70% is widely demonstrated. [15,21-24] Based on Figure S3, Supporting Information, the terms ln a and ln b in Equation (5) are in the range of -0.22 to -1.2. In contrast, the other terms in Equation (5) are much larger $(\ln(J_{\text{sc,cSi}}^t/J_{0,\text{cSi}}^t))$ that is about 33.5 and $\ln(J_{\text{sc,cSi}}/J_{0,\text{cSi}})$ is about 27.6), based on $J_{\text{sc,cSi}}$ and $J_{0,\text{cSi}}$ reported by Blakers et al. [25] for high-efficiency cSi solar cells. Therefore, the terms ln a and ln b can safely be disregarded such that $f_{
m Voc,bot} pprox f_{
m Voc,cSi}$. The term $f_{\rm Isc,bot}$ can be expressed by the following equation

$$f_{\rm Jsc,bot} = \frac{J_{\rm sc,bot}}{J_{\rm sc,bot}^{\rm t}} = \frac{J_3 + J_4 + J_5}{J_1 + J_2 + J_3} \tag{6}$$

where J_1 , J_2 , J_3 , J_4 , and J_5 refer to the current densities corresponding to the indicated spectral EQE areas in **Figure 4**. Note that in Equation (6), J_4 and J_5 only appear in the numerator, because $J_{\text{sc,bot}}^{\text{t}}$ assumes step function-like bandgaps. Equation (6) assumes that luminescence by radiative recombination in the top subcell does not influence current generation in the bottom cell. [8] Such contribution is expected to be small because the luminescence of the perovskite top cell is generally very low, certainly when operated in the maximum power point.

Figure 4 shows the measured EQE spectrum of the MWT-SHJ cell filtered by the ST-PSC-1 and its comparison to the EQE of the single-junction MWT-SHJ cell as well as the detailed-balance absorption profile. Area 1 indicates the EQE spectral difference between the single-junction and filtered cSi cell between two wavelengths corresponding to $E_{\rm g,PER}$ and cSi $E_{\rm g}$ ($E_{\rm g,cSi}$). In the

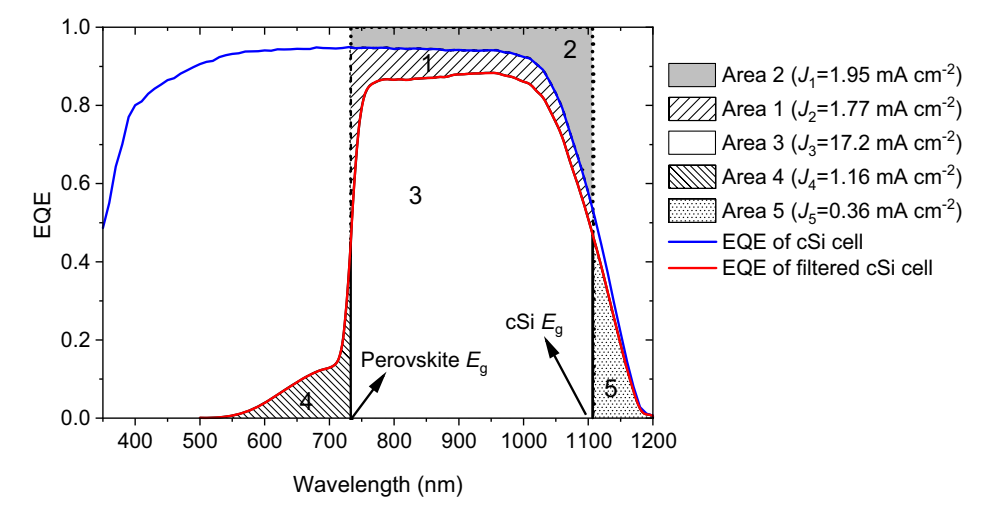


Figure 4. The EQE spectrum of the metal-wrap through silicon heterojunction (MWT-SHJ) cell filtered by an ST-PSC (specifically the cell of ST-PSC-1 shown in Table 1) in comparison to that of the single-junction cell and the detailed-balance absorption profile between two wavelengths corresponding to $E_{g,PER}$ and $E_{g,cSi}$. The AM1.5G-integrated photocurrents J_1-J_5 correspond to the different areas indicated in the EQE spectrum.

Join

www.advancedsciencenews.com www.solar-rrl.com

same wavelength range. Area 2 corresponds to the difference between the detailed-balance absorption profile and the EQE of the single-iunction cSi cell. Area 3 covers the EQE of filtered MWT-SHJ cell for photon energies (E) in the range $E_{g,PER} \ge E \ge E_{g,cSi}$. Note that the optical assumptions of the detailed-balance model for perovskite/cSi tandem calculation include the complete absorption of all the photons with higher energy than $E_{g,PER}$ for the perovskite cells and complete absorption of the photons with the energy between $E_{g,PER}$ and $E_{g,cSi}$ for the cSi cells. Area 4 refers to the number of photons that can be absorbed by the perovskite cell, but that actually pass the top cell and are then absorbed by the cSi bottom cell instead. Area 5 is related to the small absorption by the cSi cell of photons with an energy lower than $E_{g,cSi}$. Therefore, $J_1 = J_3(1/T_{NIR}^W - 1)$ accounts for the current density loss caused by the transmission of the ST-PSC. T_{NIR}^{W} is the weighted average transmittance defined by the following equation

$$T_{\text{NIR}}^{\text{W}} = \frac{\int_{E_{g,\text{CSI}}}^{E_{g,\text{PER}}} T_{\text{NIR}}(E) \Phi(E) dE}{\int_{E_{g,\text{PER}}}^{E_{g,\text{PER}}} \Phi(E) dE}$$
(7)

where $T_{\rm NIR}(E)$ is the transmittance of the perovskite top cell and $\Phi(E)$ is the photon density of the AM1.5G solar spectrum. $J_2 \approx (J_3/T_{\rm NIR}^{\rm W})(1/f_{\rm Jsc,cSi}-1)$ accounts for the additional current density loss caused by the cSi cell itself, e.g., metallic shading and parasitic absorption of the emitter and reflection. Therefore, Equation (6) is rewritten as the following equation

$$f_{\rm Jsc,bot} = \frac{J_3 + J_4 + J_5}{J_3 / (T_{\rm NIR}^{\rm W} \cdot f_{\rm Jsc,cSi})} = \alpha \cdot T_{\rm NIR}^{\rm W} \cdot f_{\rm Jsc,cSi}$$
 (8)

where $\alpha=(J_3+J_4+J_5)/J_3$. Because both J_3 and J_4 are related to the perovskite layer thickness and its bandgap energy $E_{\rm g,PER}$; also α depends on these parameters. To evaluate the value of α , the filtered EQE of the MWT-SHJ cell is calculated with validated optical modeling^[15] at different perovskite layer thickness and two different values for $E_{\rm g,PER}$. The optical structure of the ST-PSC is shown in Figure 3. Then α is calculated as shown in Figure S4, Supporting Information. The perovskite layer thickness (of 500–700 nm) was chosen in the range commonly used for (PSCs). [26–29] It turns out that α can be approximated to be a constant value of 1.13 with a relatively small standard deviation of 0.03 in the perovskite layer thickness and $E_{\rm g,PER}$ ranges used.

In addition, $\mathrm{FF}_{\mathrm{bot}}^{\mathrm{t}} \approx \mathrm{FF}_{\mathrm{cSi}}^{\mathrm{t}}$ since the FF variation caused by the small V_{oc} change in the detailed-balance model is negligible. The FF_{\mathrm{bot}} is normally higher than the FF_{cSi}, resulting from reduced series resistance losses because the filtered cSi cell generates less current than the single-junction cell. In practice, however, the difference between FF_{\mathrm{bot}} and FF_{cSi} will be very small for a high-efficiency cSi cell with optimized electrodes and its effect on cSi cell efficiency is negligible. In contrast, the J_{sc} variation plays a dominant role. Figure S5, Supporting Information, shows the FF and η measured as a function of J_{sc} for the MWT-SHJ cell used in this work. Although the FF increases at lower J_{sc} , the η of the MWT-SHJ cell is fully dominated by the change in J_{sc} as can be inferred from the clear linearity of the η with J_{sc} . Therefore, $f_{\mathrm{FF,bot}}$ approximates $f_{\mathrm{FF,cSi}}$. With Equation (5) and (8), Equation (4) can be rewritten as

Table 2. Data of 4T tandem cells from this work and the literature.

| f_{PER} | η ^t [%] | f_{cSi} | η ^t [%] | T _{NIR} [%] | E _{g,PER} [eV] | $\eta_{ m 4T}$ [%] Measured | $\eta_{ m 4T}$ [%] Calculated | Reference |
|-----------|-----------------------|-----------|-----------------------|-------------------------|----------------------------|--------------------------------|----------------------------------|-------------------------|
| 0.598 | 28.9 | 0.692 | 15.4 | 91.0 | 1.69 | 28.0 | 28.2 | ST-PSC-1 (This work) |
| 0.616 | 28.9 | 0.692 | 15.4 | 71.9 | 1.69 | 26.3 | 26.5 | ST-PSC-2 (This work) |
| 0.519 | 30.2 | 0.726 | 13.4 | 92.0 | 1.60 | 25.7 | 25.8 | [15] |
| 0.598 | 28.4 | 0.753 | 16.0 | 79.8 | 1.72 | 27.7 | 27.8 | [21] |
| 0.595 | 29.9 | 0.671 | 13.9 | 78.6 | 1.63 | 26.2 ^{a)} | 26.1 | [22] |
| 0.520 | 26.5 | 0.701 | 18.2 | 89.9 | 1.82 ^{b)} | 27.1 | 26.8 | [23] |
| 0.569 | 30.0 | 0.616 | 13.6 | 84.7 | 1.61 ^{b)} | 25.2 | 25.1 | [24] |

^{a)}Modified η when J_{sc} of the bottom cell is taken from EQE; ^{b)} $E_{g,PER}$ is recalculated from EQE in the corresponding article (Figure S6, Supporting Information) using the method reported by Krückemeier et al.^[31]

$$\eta_{\text{4T}} = f_{\text{PFR}} \cdot \eta_{\text{PFR}}^{\text{t}} + f_{\text{Voc} \, cSi} \cdot \alpha \cdot T_{\text{NIR}}^{\text{W}} \cdot f_{\text{Isc} \, cSi} \cdot f_{\text{FF} \, cSi} \cdot \eta_{\text{bot}}^{\text{t}}$$
(9)

By taking Equation (3) into Equation (9)

$$\eta_{\text{4T}} = f_{\text{PER}} \cdot \eta_{\text{PER}}^{\text{t}} + \alpha \cdot T_{\text{NIR}}^{\text{W}} \cdot f_{\text{cSi}} \cdot \eta_{\text{bot}}^{\text{t}}$$
(10)

Since f_{PER} , η_{PER}^{t} , and η_{bot}^{t} are dependent on $E_{g,PER}$, Equation (10) can be generalized to Equation (11)

$$\eta_{\text{4T}}(E_{\text{g,PER}}) = f_{\text{PER}}(E_{\text{g,PER}}) \cdot \eta_{\text{PER}}^{\text{t}}(E_{\text{g,PER}}) \\
+ \alpha \cdot T_{\text{NIR}}^{\text{W}} \cdot f_{\text{cSi}} \cdot \eta_{\text{bot}}^{\text{t}}(E_{\text{g,PER}})$$
(11)

To validate the model expressed by Equation (11), the calculated $\eta_{4\mathrm{T}}$ is compared with measured values (**Table 2**). In addition to tandem cells made in this work, Table 1 extensively lists 4T-tandem results collected from the literature. The deviation between calculated and measured $\eta_{4\mathrm{T}}$ is small, suggesting a good accuracy of Equation 11. Note that although the constant α of 1.13 was deduced on basis of the calculations for $E_{\mathrm{g,PER}}$ equal to 1.60 or 1.69 eV, it is still valid for $E_{\mathrm{g,PER}}$ up to 1.82 eV.

2.3. Maximum 4T Perovskite/cSi Tandem Efficiency with the Record Perovskite and cSi PV Technologies

In 2017, Kaneka reported a single-junction IBC cSi cell with a record efficiency of $26.7\%^{[3]}$ which corresponds to an $f_{\rm cSi}$ of 81.4% and has not been surpassed since. Therefore, this efficiency could be considered as, or close to, the practical efficiency limit of single-junction cSi PV which is also in line with predictions by Swanson in 2005. [2] In 2021, a perovskite cell with a record efficiency of 25.7% was realized. [30] These two record efficiencies of perovskite and cSi cells cannot be directly compared because the corresponding devices have different $E_{\rm g}$. However, their level of "perfection" can be inferred from the fraction of the detailed-balance efficiency. [31] The perovskite record cell is made with an $E_{\rm g}$ of 1.54 eV and realizes 82.2% of its theoretical efficiency limit which is even slightly higher than for cSi PV. [5,32,33] Since the $E_{\rm g}$ of this record perovskite cell is still

of use; OA articles are governed by the applicable Creative Commons I

www.solar-rrl.com

not in the optimal range of single-junction solar cells, an increase in efficiency might be possible in the future. However, in terms of the fraction of the detailed-balance efficiency limit, a breakthrough seems quite difficult. Therefore, a 4T tandem with the aforementioned record perovskite and cSi cells can provide a realistic estimate of the practical efficiency limit for the 4T perovskite/cSi tandem concept.

Almost all high-efficiency perovskite cells are processed with a full-area metal rear electrode, i.e., a nontransparent (NT) structure. To make the perovskite cells suitable for a 4T tandem configuration, the rear metal electrode has to be replaced by a transparent electrode, typically a TCO such as ITO, IOH, or indium zinc oxide (IZO). Replacement of a metal electrode with an optimized transparent electrode will cause negligible $V_{\rm oc}$ and FF losses (Figure S7, Supporting Information). However, a loss in $J_{\rm sc}$ is difficult to prevent since the metal electrode offers effective back reflection which doubles the optical path for effective light absorption. **Figure 5** compares the optically simulated $J_{\rm sc}$

of an NT-PSC to that of an ST-PSC at different perovskite layer thickness. The simulated J_{sc} is calculated based on the absorption of perovskite layer (A_{PER}) with the following equation

$$J_{\rm sc}(E) = e \int_0^\infty \Phi(E) A_{\rm PER}(E) dE \tag{12}$$

where $\Phi(E)$ is the photon flux of the standard AM1.5G solar spectrum. Here, a collection efficiency of 1 is assumed for photon-generated carriers in the perovskite layer. The difference in $J_{\rm sc}$ between cells with and without a metal electrode is very pronounced when the perovskite layer is thin, but becomes smaller when the perovskite layer thickness increases. Figure 5 suggests that the relative difference in $J_{\rm sc}$ between NT-PSCs and ST-PSCs is not expected to go below 2% and, hence, the value of 2% is taken as a minimal $J_{\rm sc}$ loss after an ST-PSC is optimized from the corresponding NT-PSC for calculation of the practical efficiency limit.

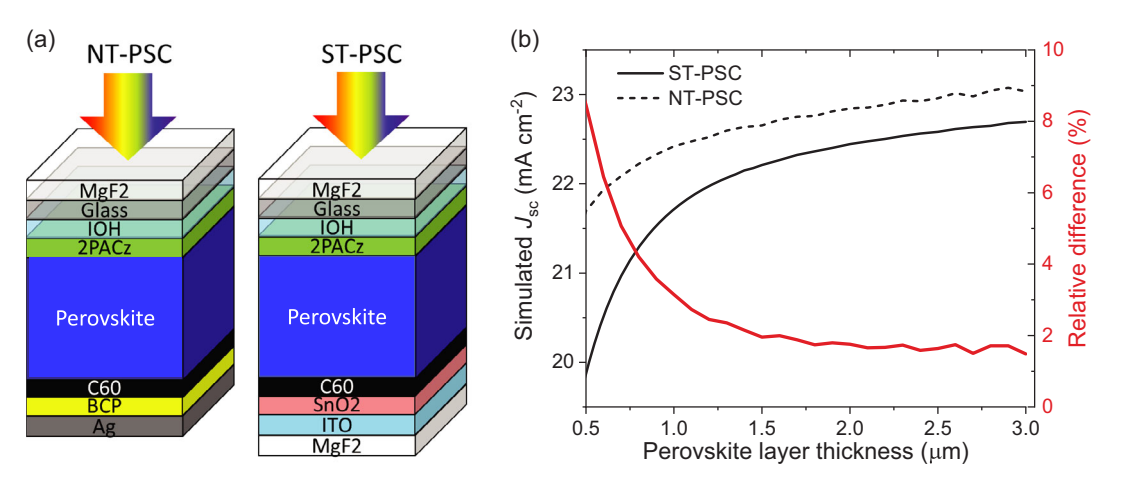


Figure 5. a) Optical structure of an NT-PCS and an ST-PSC. b) Optically simulated J_{sc} as a function of perovskite layer thickness, for the perovskite absorber used in this work and assuming a carrier collection efficiency of 1.

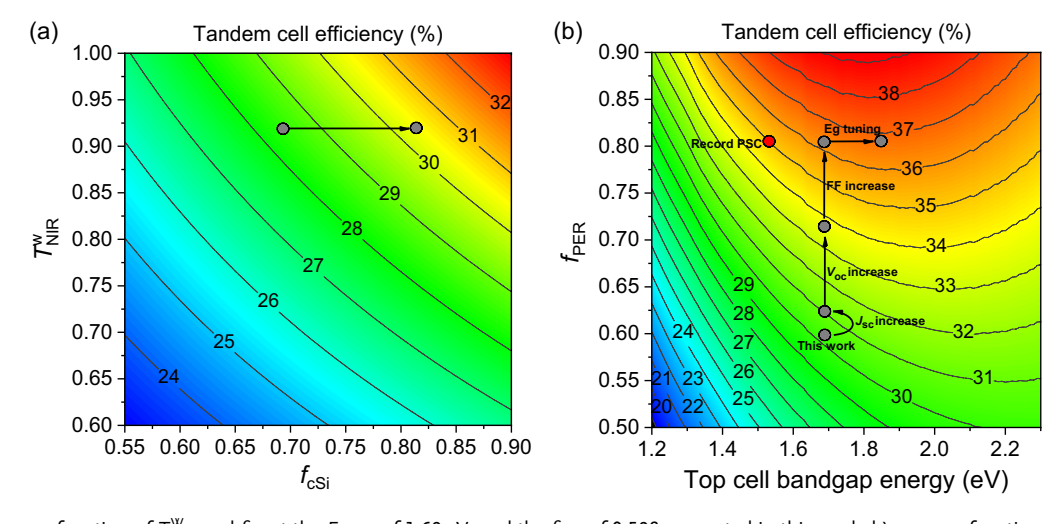


Figure 6. a) η_{4T} as a function of T_{NIR}^{W} and f_{cSi} at the $E_{g,PER}$ of 1.69 eV, and the f_{PER} of 0.598 presented in this work. b) η_{4T} as a function of $E_{g,PER}$ and f_{PER} starting with the record T_{NIR}^{W} of 92% and the record f_{cSi} of 81.4%.

Solar

www.advancedsciencenews.com www.solar-rrl.com

Figure 6 shows the highest attainable $\eta_{\rm 4T}$, when both the perovskite and the cSi subcells in this work can be optimized to the level of the corresponding record devices, in other words, the same faction of the detailed-balance performance limit as the record devices. The calculation is based on Equation (11) that has been validated with data from Table 2. Figure 6a shows the tandem efficiency as the function of $T_{\rm NIR}^{\rm W}$ and $f_{\rm cSi}$. Due to the parasitic absorption of the TCO in the NIR and reflection caused by the layer stack of perovskite cells, there is a marginal increase of $T_{\rm NIR}^{\rm W}$. The $T_{\rm NIR}^{\rm W}$ of about 92% is the highest demonstrated in the literature so far. [15] A large enhancement of $\eta_{\rm 4T}$, which is about absolute 2.4%, can originate from the increase of $f_{\rm cSi}$ from 69.2% of the MWT-SHJ cell employed in this work to 81.4% of the world-record cSi cell.

Figure 6b indicates the possible further improvement of η_{4T} when the ST-PSC from this work can be further optimized. Table S1, Supporting Information, shows the comparison of the ST-PSC-1 in this work to the record PSCs. Since the two cells have very different E_g , direct comparison of the J-V parameters is not meaningful, and thereby they are compared in terms of the fraction of the detailed-balance performance limit of each single J-V parameter. Note that the J_{sc} of the ST-PSC-1 cell is already quite close to that of the record cell, taking into account the minimum loss of 2% relative due to the absence of effective back reflection as previously shown in Figure 5. The η_{4T} can increase by about 1% absolute when $f_{\rm isc, PER}$ increases from 87.6% to 91.1%. More importantly, further increase of $f_{\text{voc,PER}}$ from the current 82.2% to the record 94.9% can lead to about 3% absolute η_{4T} enhancement. The possibility of reaching high V_{oc} for widebandgap perovskite is supported by the recent work from Liu et al. They reported a high V_{oc} of 1.35 V for perovskite cells with the E_g of 1.725 eV, corresponding to 94.7% of its theoretical $V_{\rm oc}$ limit. With a further increase of $f_{\rm FF,PER}$ from 83.6% to 92.3%, the 4T tandem can reach a η_{4T} of 36%. In 2020, Al-Ashouri et al. $^{[35]}$ demonstrated a PSC with a $E_{\rm g}$ of 1.68 eV and an FF of 84%, which corresponds to an $f_{\rm FF,PER}$ of 92.4%, implying that the FF of the wide-bandgap perovskite cells is already able to reach the level of the record perovskite cell with respect to approaching the detailed-balance limit. The η_{4T} could reach about 36.8% if the perovskite E_g can be tuned to its optimum of around 1.85 eV, while f_{PER} retains the same.

Even though the $E_{\rm g}$ of the record perovskite cell deviates considerably from the optimum for a tandem cell with cSi, about 35% tandem efficiency could be attainable with this $E_{\rm g}$ if the existing record perovskite and cSi cells could be adapted for the 4T tandem configuration. This shows once more the flexibility of the 4T tandem configuration to the $E_{\rm g}$ of the top cell. Note that the optimal $E_{\rm g}$ of a perovskite cell is highly dependent on its $f_{\rm PER}$. In fact, the optimal $E_{\rm g}$ increases rapidly as $f_{\rm PER}$ decreases. The $\eta_{\rm 4T}$ gain from $E_{\rm g}$ optimization is much higher at low $f_{\rm PER}$.

In this work, we focused on the efficiency potential of lab-scale cells. Inevitable losses from lab-scale cells to a large-area module will mainly be caused by layer inhomogeneity, the tradeoff between absorption and resistance losses of the TCO, and the dead-area fraction. Recently, an over 25%-efficient 4T perovskite/Si tandem device on a 6-inch area has been presented by Zardetto et al. [36] A comparison of this result with Table 1

demonstrates that the gap between lab-scale cells and large-area devices can be minimized.

3. Conclusion

In this contribution, a method for calculating the 4T perovskite/ cSi tandem efficiency is proposed and validated with experimental results as well as several results from the literature. The experimental input data which are required by this calculation include the efficiencies of the ST-PSC and the cSi cells measured at AM1.5G 1 sun condition, and the EQE and transmittance spectra of the ST-PSC. First, the $E_{g,PER}$ is determined from the EQE of the ST-PSC^[31] Second, the theoretical efficiency values of $\eta_{\rm PER}^{\rm t}$, η_{cSi}^{t} , and η_{bot}^{t} are calculated (Section 1, Supporting Information), followed by the calculation of f_{PER} and f_{cSi} (Equation (1)). Third, $T_{\text{NIR}}^{\text{W}}$ can be obtained based on Equation (7). At last, the $\eta_{4\text{T}}$ can be calculated with Equation (11). We show that the calculated efficiency deviates not more than 1% relative to actual device measurements. This method can clearly reveal how the performance of the top and bottom cells, transmittance of top cells, and perovskite E_{σ} influences the tandem cell performance and can be used for tandem device optimization. Experimentally, a high tandem efficiency of 28.0% is achieved with the 4T perovskite/cSi tandem configuration. Our calculations show that it is possible to reach about 36% tandem efficiency when both perovskite top and cSi bottom cells can be optimized to the level of their current record devices. Furthermore, it shows in which direction the optimization should take place by evaluating which among the J-V parameters, E_g , or transmittance have more room for improvement and more impact on the tandem performance. Using this method we conclude that an efficiency of about 36% can be considered the practical efficiency limit for 4T tandem perovskite/cSi solar cells.

4. Experimental Section

Preparation of Precursor Solutions: All materials were purchased from commercial sources and used as received unless stated otherwise. Prior to the preparation of perovskite precursor solutions, stock solutions of PbI₂, PbBr₂, and CsI were made, stored in the glovebox, and repeatedly used. PbI₂ (5532 mg) (TCI Chemicals, 99.99% trace metal basis) was dissolved in a mixture of DMF (7.2 mL) (Sigma Aldrich, 99.8%) and DMSO (0.8 mL) (Sigma Aldrich, 99.9%), PbBr₂ (1101 mg) (TCI Chemicals, >98.0%) in a mixture of DMF (1.8 mL) and DMSO (0.2 mL), and CsI (779.4 mg) (Sigma-Aldrich, 99.999% trace metal basis) in DMSO (2 mL). Right before making the perovskite precursor solution, the PbI₂ and PbBr₂ stock solutions were heated to 150 °C for 15 min and then cooled to room temperature. The perovskite precursor solution was prepared by mixing formamidinium iodide (FAI) (Greatcell Solar Materials) (283.2 mg), methylammonium bromide (MABr) (Greatcell Solar Materials) (36.88 mg) with a mixture of the PbI₂ stock solution (1077 μ L), the PbBr₂ stock solution (454.3 μ L), and the CsI stock solution (69.3 µL) to realize the nominal perovskite composition of $Cs_{0.05}FA_{0.79}MA_{0.16}Pb(I_{0.75}Br_{0.25})_3$. As HTL, [2-(9H-carbazol-9-yl)ethyl] phosphonic acid (2PACz) (TCI Chemicals) was used which was dissolved in anhydrous ethanol (Merck Millipore) with 30 min of sonication at a concentration of 0.33 mg mL⁻¹.

Device Fabrication. Prepatterned ITO or IOH covered glass substrates were cleaned sequentially with soap water, deionized water, and isopropanol in an ultrasonic bath. Each step takes 5 min. After they were treated in UV ozone for 30 min, the substrates were transferred into the glovebox

www.advancedsciencenews.com

www.solar-rrl.com

for spin coating of the HTL and the perovskite. For HTL deposition, 2PACz solution (120 µL) was first dripped slowly on the substrate to fully cover the substrate surface. After about 30 s, spin coating started at 3000 rpm and lasted for 30 s, immediately followed by annealing at 100 °C for 10 min. The perovskite layer was deposited with antisolvent methods. The spin coating of perovskite started with 1000 rpm for 10 s and accelerated to 5000 rpm for 20 s. Chlorobenzene (CB) was dripped onto the perovskite film at 23 s. After spin coating, the perovskite film was immediately annealed at 150 °C for 10 min. On top of perovskite, C₆₀ (SES Research, 99.95%) was thermally evaporated, followed by a SnO₂ layer, deposited with spatial atomic layer deposition. Afterward, sputtered ITO and evaporated Ag grids were processed as rear electrodes. Finally, antireflective MgF2 layers were evaporated on both the glass and the top electrode. The details about the MWT-SHJ cells are reported in our previous publication.[37]

Characterization: I-V characteristics of the PSCs were measured with a WACOM solar simulator which was calibrated with a Si reference cell purchased from Fraunhofer ISE. The cell area of 9 mm² is defined by a stainless-steel shadow mask. The scan speed was 200 mV s⁻¹, controlled by a Keithley 2400 source-measure unit. The J-V of the cSi cells was measured with full-area illumination using a Neonsee solar simulator. The EQE of all solar cells was measured with a setup from ReRa Solutions BV. Transmittance spectra were measured with an Agilent Carry 5000 spectrophotometer with an integrating sphere. The top and bottom cells are measured separately. Therefore, it is not necessary to have the solar simulator fit the subcell spectra simultaneously, and mismatch factors can be chosen separately for perovskite and cSi single-junction cells.

Measurement Protocol for 4T Perovskite-cSi Tandem Cells: 1) J-V of perovskite top cell is directly measured, using a black background; 2) single-junction cSi cells are measured with a solar simulator to obtain $J_{\text{sc_IV}}$; 3) EQE measurement is taken at the active area of cSi cells to obtain J_{sc} EOE; 4) a shadow loss factor (f) of cSi cells is determined by $J_{\text{sc IV}}/J_{\text{sc EOE}}$. The main reason for introducing f is that the EQE is measured in the active area of cSi cells, while the J-V is a full-area measurement. By introducing f, the metallic shading fraction is taken into account in the EQE measurement of the cSi cells; 5) EQE measurement is taken at the active area of cSi cells filtered by the perovskite cell to obtain $J_{\text{sc_filtered}}$. The J_{sc} of cSi bottom cells (J_{sc_bottom}) is $f \times J_{sc_filtered}$; 6) IV of cSi cells is measured with gray filters to obtain V_{oc} , FF, and efficiency at J_{sc_bottom} ; and 7) the sum of perovskite top and cSi bottom cell efficiencies is the 4T tandem cell efficiency. Note that instead of the gray filters used in step 6, a color cut-off filter resembling the bandgap of perovskites would be better. However, gray filters are good enough when the distribution of the generation profile has negligible impacts on cell performance, which is the case for the high-efficiency cSi cells as used in this work.

Supporting Information

Supporting Information is available from the Wiley Online Library or from the author.

Acknowledgements

The authors acknowledge Solliance, a partnership of R&D organizations from The Netherlands, Belgium, and Germany working in thin-film photovoltaic solar energy. The authors acknowledge funding from the Ministry of Education, Culture, and Science (Gravity program 024.001.035) and from the Netherlands Organization for Scientific Research (NWO) through the Joint Solar Programme III (Project 680.91.011) and the NWO Spinoza grant.

Conflict of Interest

The authors declare no conflict of interest.

Data Availability Statement

The data that support the findings of this study are available from the corresponding author upon reasonable request.

Keywords

crystalline silicon, detailed-balance, four-terminal tandem cells, perovskites, solar cells

> Received: October 12, 2022 Revised: November 16, 2022 Published online:

- [1] M. Fischer, M. Woodhouse, S. Herritsch, J. Trube, International Technology Roadmap for Photovoltaic (ITRPV) 2020 Results (Ed: VDMA e. V. Photovoltaic Equipment), 12th ed., Frankfurt am Main, Germany.
- [2] R. M. Swanson, in Conf. Rec. Thirty-First IEEE Photovoltaics Specialist Conf. 2005, IEEE, Piscataway, NJ 2005, pp. 889-894.
- [3] K. Yoshikawa, H. Kawasaki, W. Yoshida, T. Irie, K. Konishi, K. Nakano, T. Uto, D. Adachi, M. Kanematsu, H. Uzu, K. Yamamoto, Nat. Energy **2017**. 2. 17032.
- [4] Z. Yu, M. Leilaeioun, Z. Holman, Nat. Energy 2016, 1, 16137.
- [5] B. Ehrler, E. Alarcón-Lladó, S. W. Tabernig, T. Veeken, E. C. Garnett, A. Polman, ACS Energy Lett. 2020, 5, 3029.
- [6] A. Polman, M. Knight, E. C. Garnett, B. Ehrler, W. C. Sinke, Science. 2016. 352. 307.
- [7] S. Rühle, Sol. Energy 2016, 130, 139.
- [8] M. H. Futscher, B. Ehrler, ACS Energy Lett. 2016, 1, 863.
- [9] S. Kim, T. T. Trinh, J. Park, D. P. Pham, S. Lee, H. B. Do, N. N. Dang, V.-A. Dao, J. Kim, J. Yi, Sci. Rep. 2021, 11, 15524.
- [10] J. Werner, B. Niesen, C. Ballif, Adv. Mater. Interfaces 2018, 5, 1700731.
- [11] T. Leijtens, K. A. Bush, R. Prasanna, M. D. McGehee, Nat. Energy 2018, 3, 828.
- [12] S. Essig, S. Ward, M. A. Steiner, D. J. Friedman, J. F. Geisz, P. Stradins, D. L. Young, Energy Procedia 2015, 77, 464.
- [13] P. Manshanden, G. Coletti, V. Rosca, M. J. Jansen, K. M. de Groot, G. J. de Graaff, M. Creatore, K. Datta, R. Janssen, L. Simurka, D. Zhang, M. Najafi, V. Zardetto, I. Dogan, H. Fledderus, S. C. Veenstra, in 38th European Photovoltaics Solar Energy Conf. and Exhibition, Lisbon, Portugal, 2021, pp. 363-365.
- [14] NREL, Best Research-Cell Efficiency Chart, 2022. https://www.nrel. gov/pv/assets/pdfs/best-research-cell-efficiencies-rev220630.pdf (accessed: August 2022).
- [15] D. Zhang, M. Najafi, V. Zardetto, M. Dörenkämper, X. Zhou, S. Veenstra, L. J. Geerligs, T. Aernouts, R. Andriessen, Sol. Energy Mater. Sol. Cells 2018, 188, 1.
- [16] M. Semma, K. Gotoh, Y. Kurokawa, N. Usami, in 2020 47th IEEE Photovoltaics Specialist Conf., IEEE, Piscataway, NJ 2020, pp. 0124-0127.
- [17] L. Zhao, C. L. Zhou, H. L. Li, H. W. Diao, W. J. Wang, Phys. Status Solidi 2008, 205, 1215.
- [18] J. Werner, L. Barraud, A. Walter, M. Bräuninger, F. Sahli, D. Sacchetto, N. Tétreault, B. Paviet-Salomon, S.-J. Moon, C. Allebé, M. Despeisse, S. Nicolay, S. De Wolf, B. Niesen, C. Ballif, ACS Energy Lett. 2016, 1,
- [19] S. De Wolf, J. Holovsky, S. Moon, P. Löper, B. Niesen, M. Ledinsky, F. Haug, J. Yum, C. Ballif, J. Phys. Chem. Lett. 2014, 5, 1035.
- [20] D. Zhang, I. A. Digdaya, R. Santbergen, R. A. C. M. M. van Swaaij, P. Bronsveld, M. Zeman, J. A. M. van Roosmalen, A. W. Weeber, Sol. Energy Mater. Sol. Cells 2013, 117, 132.



Solar

www.advancedsciencenews.com www.solar-rrl.com

- [21] T. Duong, H. Pham, T. C. Kho, P. Phang, K. C. Fong, D. Yan, Y. Yin, J. Peng, M. A. Mahmud, S. Gharibzadeh, B. A. Nejand, I. M. Hossain, M. R. Khan, N. Mozaffari, Y. Wu, H. Shen, J. Zheng, H. Mai, W. Liang, C. Samundsett, M. Stocks, K. McIntosh, G. G. Andersson, U. Lemmer, B. S. Richards, U. W. Paetzold, A. Ho-Ballie, Y. Liu, D. Macdonald, A. Blakers, J. Wong-Leung, T. White, K. Weber, K. Catchpole, Adv. Energy Mater. 2020, 10, 1903553.
- [22] A. Rohatgi, K. Zhu, J. Tong, D. H. Kim, E. Reichmanis, B. Rounsaville, V. Prakash, Y.-W. Ok, *IEEE J. Photovoltaics* 2020, 10, 417.
- [23] M. Jaysankar, S. Paetel, E. Ahlswede, U. W. Paetzold, T. Aernouts, R. Gehlhaar, J. Poortmans, Prog. Photovoltaics Res. Appl. 2019, 27, 733.
- [24] C. O. Ramírez Quiroz, Y. Shen, M. Salvador, K. Forberich, N. Schrenker, G. D. Spyropoulos, T. Heumüller, B. Wilkinson, T. Kirchartz, E. Spiecker, P. J. Verlinden, X. Zhang, M. A. Green, A. Ho-Baillie, C. J. Brabec, J. Mater. Chem. A 2018, 6, 3583.
- [25] A. Blakers, N. Zin, K. R. McIntosh, K. Fong, Energy Procedia 2013, 33, 1.
- [26] P. Cui, D. Wei, J. Ji, H. Huang, E. Jia, S. Dou, T. Wang, W. Wang, M. Li, Nat. Energy 2019, 4, 150.
- [27] M. Najafi, V. Zardetto, D. Zhang, D. Koushik, M. S. Dörenkämper, M. Creatore, R. Andriessen, P. Poodt, S. Veenstra, Sol. RRL 2018, 2, 1800147.
- [28] X. Zhang, X. Chen, Y. Chen, N. A. Nadege Ouedraogo, J. Li, X. Bao, C. B. Han, Y. Shirai, Y. Zhang, H. Yan, Nanoscale Adv. 2021, 3, 6128.
- [29] H. Tan, A. Jain, O. Voznyy, X. Lan, F. P. García de Arquer, J. Z. Fan, R. Quintero-Bermudez, M. Yuan, B. Zhang, Y. Zhao, F. Fan, P. Li, L. N. Quan, Y. Zhao, Z.-H. Lu, Z. Yang, S. Hoogland, E. H. Sargent, Science 2017, 355, 722.

- [30] H. Min, D. Y. Lee, J. Kim, G. Kim, K. S. Lee, J. Kim, M. J. Paik, Y. K. Kim, K. S. Kim, M. G. Kim, T. J. Shin, S. Il Seok, *Nature* 2021, 598, 444.
- [31] L. Krückemeier, U. Rau, M. Stolterfoht, T. Kirchartz, Adv. Energy Mater. 2020, 10, 1902573.
- [32] M. A. Green, E. D. Dunlop, J. Hohl-Ebinger, M. Yoshita, N. Kopidakis, K. Bothe, D. Hinken, M. Rauer, X. Hao, *Prog. Photovoltaics Res. Appl.* 2022. 30, 687.
- [33] M. Jeong, I. W. Choi, E. M. Go, Y. Cho, M. Kim, B. Lee, S. Jeong, Y. Jo, H. W. Choi, J. Lee, J.-H. Bae, S. K. Kwak, D. S. Kim, C. Yang, *Science* 2020, 369, 1615.
- [34] Z. Liu, J. Siekmann, B. Klingebiel, U. Rau, T. Kirchartz, Adv. Energy Mater. 2021, 11, 2003386.
- [35] A. Al-Ashouri, E. Köhnen, B. Li, A. Magomedov, H. Hempel, P. Caprioglio, J. A. Márquez, A. B. Morales Vilches, E. Kasparavicius, J. A. Smith, N. Phung, D. Menzel, M. Grischek, L. Kegelmann, D. Skroblin, C. Gollwitzer, T. Malinauskas, M. Jošt, G. Matič, B. Rech, R. Schlatmann, M. Topič, L. Korte, A. Abate, B. Stannowski, D. Neher, M. Stolterfoht, T. Unold, V. Getautis, S. Albrecht, *Science* 2020, 370, 1300.
- [36] V. Zardetto, L. Simurka, D. Zhang, W. Verhees, G. Lucarelli, H. Fledderus, M. Najafi, I. Dogan, D. Roosen-Melsen, P. Manshanden, G. Coletti, V. Gevaerts, S. Veenstra, in 8th World Conf. Photovolt. Energy Convers., Milan, Italy, 2022, oral presentation (2CO.2.3).
- [37] R. D. Beauchemin, D. M. Wilt, P. E. Hausgen, in 2017 IEEE 44th Photovoltaics Specialist Conf., IEEE, Piscataway, NJ 2017, pp. 102–106.